




Structural complexity of snapshots of two-dimensional Fermi-Hubbard systemsEduardo Ibarra-García-Padilla ^{1,2,*}, Stephanie Striegel,² Richard T. Scalettar ¹ and Ehsan Khatami ^{2,†}¹*Department of Physics and Astronomy, University of California, Davis, Davis, California 95616, USA*²*Department of Physics and Astronomy, San José State University, San José, California 95192, USA*

(Received 17 January 2024; revised 15 April 2024; accepted 16 April 2024; published 6 May 2024)

The development of quantum gas microscopy for two-dimensional optical lattices has provided an unparalleled tool to study the Fermi-Hubbard model (FHM) with ultracold atoms. Spin-resolved projective measurements, or snapshots, have played a significant role in quantifying correlation functions, theory verification, and thus the uncovering of underlying physical phenomena such as antiferromagnetism at commensurate filling on bipartite lattices and other charge and spin correlations, as well as dynamical properties at various densities. Here we employ a recent concept, the multiscale structural complexity, and show that when computed for the snapshots (of single spin species, local moments, or total density) it can provide a theory-free property, immediately accessible to experiments. Specifically, after benchmarking results for Ising and XY models, we study the structural complexity of snapshots of the repulsive FHM in the two-dimensional square lattice as a function of doping and temperature. We generate projective measurements using determinant quantum Monte Carlo and compare their complexities against those from the experiment. We demonstrate that these complexities are linked to relevant physical observables such as the entropy and double occupancy. Their behaviors capture the development of correlations and relevant length scales in the system. We provide an open-source code in PYTHON which can be implemented into data analysis routines in experimental settings for the square lattice.

DOI: [10.1103/PhysRevA.109.053304](https://doi.org/10.1103/PhysRevA.109.053304)**I. INTRODUCTION**

The Fermi-Hubbard model (FHM) is of great importance in describing the electronic properties of strongly correlated materials. It accurately captures some of their key characteristics and it exhibits a number of canonical phases of matter, hosting a metal-to-insulator crossover and magnetic and charge order in the two-dimensional (2D) square lattice, and is extensively researched in relationship to d -wave superconductivity [1–6].

One of the major accomplishments in quantum simulation has been the precise engineering of the FHM with ultracold atoms in optical lattices. These exhibit flexible tunability of the kinetic and interaction energies, as well as the lattice filling or even the lattice geometry [7–17]. In lower-dimensional lattices, i.e., one and two dimensions, quantum gas microscopy has provided direct observation of correlations beyond nearest neighbors through real-space imaging of spin-resolved projective measurements [18–28]. These results have yielded profound insights into the phase diagram [29], in particular regarding antiferromagnetism, and how spin correlations are affected by the presence of holes at intermediate temperatures.

Despite these great achievements, many questions remain open about the model in two dimensions, in particular those pertaining to the pseudogap, strange metal, and possible superconducting regions, where complex patterns and competing orders emerge that are hard to describe quantitatively [30–33]. One possible route to extract physical information

from projective measurements in an unbiased way, where such quantitative descriptions are difficult, is by enlisting the help of machine learning or other data-driven techniques [34]. For example, an early application of supervised learning aimed to detect the onset of the pseudogap phase upon doping in experimental snapshots [35]. In another study, kernels of a convolutional neural network, trained to distinguish experimental snapshots taken at high and low temperatures, were used to analyze correlations that develop in the system at low temperatures, including those at dopings relevant to the strange metal phase [36,37]. Machine learning has also been successfully exploited to obtain the relation between the ground-state energy and the density [38].

In this work we focus on a recently introduced unbiased measure, called multiscale structural complexity [39], which is based on dissimilarity of patterns at different scales and uses ideas from the renormalization-group flow to aggregate information about different scale correlations present in the system. So far, it has been used for analyzing snapshots of 1D classical and quantum systems [40], including systems out of equilibrium [41]. It has also been shown to be capable of detecting phase transitions to and from the off-diagonal bond-density-wave ordered phase of the half-filled extended FHM in one dimension despite only employing diagonal (density) snapshots [42]. Given the large data sets attainable in experiments with quantum gas microscopes, we demonstrate that the structural complexity can be an immediately useful tool to analyze Fermi-Hubbard snapshots.

We first apply the structural complexity technique to classical models of magnetism to build an intuition of what the dissimilarities and the complexities capture. We then study the structural complexity of the repulsive FHM in the 2D square

*edibarra@ucdavis.edu

†ehsan.khatami@sjsu.edu

lattice at intermediate coupling (where the on-site interaction equals the noninteracting bandwidth) as a function of hole doping δ and temperature T . This value of the interaction is where the antiferromagnetic correlations are maximal at commensurate filling and therefore allows for a good comparison against classical models as well as setting the stage for the study of the doped system. On the theory side, we perform determinant quantum Monte Carlo (DQMC) [43,44] simulations, from which spin-resolved, local moment, and density snapshots are generated [45]. We compare their complexities against those from experimental data and demonstrate they are directly linked to relevant physical observables such as the entropy and the double occupancy. Their behaviors illustrate the extent to which correlations arise and capture relevant length scales in the system.

The remainder of this paper is organized as follows. In Sec. II we present the models studied and the methods used. In Sec. III we present our main findings, first results for classical models, followed by those for the FHM. Section IV summarizes our findings and presents an outlook for future studies.

II. MODEL AND METHODS

A. Classical spin models

Since our main objective is to work with quantum gas microscope snapshots of Fermi-Hubbard models, which are images with 0's and 1's as the pixel values, we first aim to gain some intuition about the structural complexity and the dissimilarities measure in well-known scenarios. For this reason, we perform Monte Carlo simulations of classical spin models [46] in two dimensions,

$$H = -J \sum_{\langle i,j \rangle} \mathbf{s}_i \cdot \mathbf{s}_j = -J \sum_{\langle i,j \rangle} \cos(\theta_i - \theta_j), \quad (1)$$

in order to obtain and work with classical snapshots of spins. Here \mathbf{s}_i is the spin vector at site i and $\langle \dots \rangle$ indicates a sum over nearest neighbors. We focus on the ferromagnetic (FM) Ising model ($J > 0$, $\theta = \pm\pi/2$), the antiferromagnetic (AFM) Ising model ($J < 0$, $\theta = \pm\pi/2$), and the FM XY model ($J > 0$, $\theta \in [0, 2\pi)$). Although the location of the critical temperature is the same for the FM and AFM Ising models, $T_c/J = 2.269$, the magnetic orderings (and thus the relevant patterns in snapshots) are different and therefore one expects the behavior of the structural complexities to be different as well.

On the other hand, the 2D FM XY model does not have an order parameter, nor does it exhibit long-range order. Rather, it has a finite-temperature Berezinskii-Kosterlitz-Thouless (BKT) transition at $T_c/J = 0.88$. In this model, vortices are the topologically stable configurations and the transition is characterized by the binding-antibinding of pairs of vortices with opposite vorticity. Due to these fundamental differences, exploring this model will yield relevant information on what the complexity measures capture in the presence of more intricate patterns and topological phase transitions. It is worth noting as well that the transition into a superfluid phase in the 2D attractive FHM at generic fillings is in the BKT class [47], so an understanding of the structural complexity in the

XY model could be directly relevant to future studies of the former model as well.

B. Fermi-Hubbard model and DQMC

We are mainly interested in investigating the FHM

$$H = -t \sum_{\langle i,j \rangle, \sigma} (c_{i\sigma}^\dagger c_{j\sigma} + \text{H.c.}) + U \sum_i n_{i\uparrow} n_{i\downarrow} - \mu \sum_{i,\sigma} n_{i\sigma}, \quad (2)$$

where $c_{i\sigma}^\dagger$ ($c_{i\sigma}$) is the creation (annihilation) operator for a fermion with spin flavor $\sigma = \uparrow, \downarrow$ on site $i = 1, 2, \dots, N$ in a 2D square lattice, N denotes the number of lattice sites, $n_{i\sigma} = c_{i\sigma}^\dagger c_{i\sigma}$ is the number operator for flavor σ , t is the nearest-neighbor hopping amplitude, and U is the interaction strength. We work in the grand canonical ensemble and use the chemical potential μ to adjust the fermion density. We set $\hbar = k_B = 1$ throughout the paper and consider the $U > 0$ (repulsive) case.

In this work we generate snapshots of projective measurements in 10×10 lattices using the method described in Refs. [45,48], in which nested componentwise direct sampling of fermion pseudodensity matrices is used to generate an ensemble of pseudosnapshots, which, when reweighted, is equivalent to an ensemble of projective measurements of the occupation numbers. The procedure introduces a weight associated with each snapshot, which for all the cases we consider here is more or less uniform among snapshots and we therefore ignore it for simplicity. We use DQMC with a Trotter step of $\Delta\tau = 0.05t$. The projective measurements correspond to the spin-resolved densities $n_{i\sigma}$ in the lattice, from which the local moment $m_i^z = |n_{i\uparrow} - n_{i\downarrow}|$ and the total density $n_i = n_{i\uparrow} + n_{i\downarrow}$ are constructed. We apply point-group symmetries to increase the number of samples eightfold.

C. Structural complexity

The qualitative concept of the complexity of patterns, systems, and processes is inherent to human perception and plays an important role in natural and social sciences. A precise mathematical description was given recently [39] which formulates a single unique number that characterizes the structural complexity of an image. This number is obtained via a series of coarse-graining steps (as is done in renormalization-group calculations). In each step, information from different scales present in the system aggregates. Formally, the structural complexity \mathcal{C}_0 is defined as

$$\mathcal{C}_0 = \sum_{k=0}^{k_{\max}-1} D_k = \sum_{k=0}^{k_{\max}-1} \left| O_{k+1,k} - \frac{1}{2}(O_{k+1,k+1} + O_{k,k}) \right|, \quad (3)$$

where k_{\max} is the total number of coarse-graining steps and

$$O_{k,p} = \frac{1}{N} \sum_{i=1}^N u_i^{(k)} u_i^{(p)} \quad (4)$$

is the overlap function, where the image has N pixels and $u_i^{(k)}$ corresponds to the value of the pixel at site i at coarse-graining step k . The coarse-graining procedure using a $\Lambda \times \Lambda$ window and the calculation of the overlaps is depicted in Fig. 1. D_k is the dissimilarity at coarse-graining step k . It contains cor-

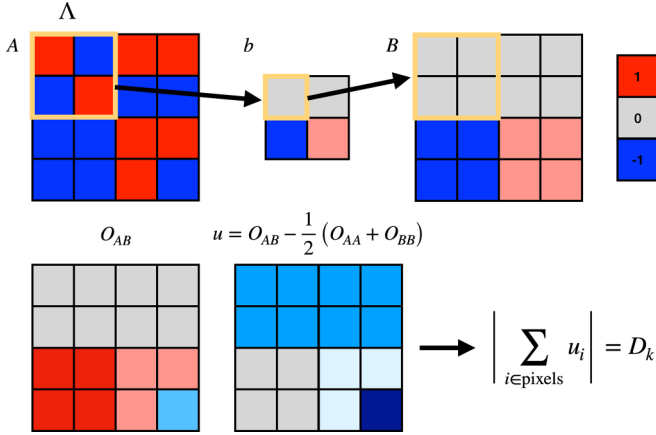


FIG. 1. Structural complexity procedure. An image A is coarse grained using a $\Lambda \times \Lambda$ window. The resulting image after coarse graining corresponds to image b , which is then resized to its original size (image B). Overlaps between images are computed by taking the dot product of the arrays. Here we illustrate the pixel-by-pixel product for the overlap between A and B (O_{AB}) and the pixel-by-pixel result for the differences between overlaps ($O_{AB} - \frac{1}{2}[O_{AA} + O_{BB}]$). Performing a sum over pixels and taking the absolute value of the result corresponds to the dissimilarity D_k .

relations that extend up to a linear size of Λ^k in the original image and measures how different the images at consecutive coarse-graining steps k and $k + 1$ are. Here we set $\Lambda = 2$. As we will see later, it is also useful to define $C_1 = C_0 - D_0$, i.e., we start the sum in Eq. (3) at $k = 1$ rather than $k = 0$. We will also see that the contributions fall off rather rapidly with k , so in practice only a limited number of terms need be considered.

This definition of the complexity reflects the intuitive sense of what corresponds to a more complex pattern in general, but also has been used specifically to detect finite- T phase transitions in models such as the classical ferromagnetic Ising model [39], to detect quantum phase transitions in the 1D extended FHM [42], and to distinguish quantum states in one-dimensional qubit chains [40]. In contrast to numerically expensive n -point correlation functions or neural network learning techniques to detect phase boundaries, the structural complexity offers a simple, unbiased, and numerically cheaper technique to do so.

To apply the technique to our DQMC snapshots, we tile a region of space using 256×256 of them, which allows us to perform the coarse-graining procedure up to nine times ($k_{\max} = 9$). In addition, we compare our results against experimental data where possible, for which a similar tessellation procedure is performed. These correspond to the data used in Ref. [36].

III. RESULTS

A. Classical models

1. Hamiltonians with \mathcal{Z}_2 symmetry

In Fig. 2(a) we show the temperature dependence of the structural complexity of the FM Ising model. Our results are in agreement with Ref. [39] and the critical temperature, deduced from the location of the rapid drop in C_0 or C_1 or the peak in their derivatives, is in excellent agreement

with the exact result. We can gain further understanding about the inner workings of the complexity measure by looking at the dissimilarities as a function of the coarse-graining step k [Fig. 2(b)]. At high temperatures in the disordered phase, D_k falls off rapidly with k . As the temperature is lowered to near, but still above, the transition, D_k decays much more slowly, with nonvanishing values even at large values of k , illustrating the existence of correlations between far regions in the model. Finally, in the ordered phase, D_k is mostly small and vanishes quickly at all k by decreasing T . This makes sense since in a perfect ferromagnet, coarse-graining does not lead to a different image.

In contrast to the FM case, where C_0 starts at a finite but constant value and then rapidly falls off to zero below the critical temperature, we find that in the AFM Ising model, C_0 remains constant at all temperatures, as can be seen in Fig. 2(c). In order to understand this, let us analyze two limiting cases. At infinite temperature, i.e., in the fully disordered phase (where each spin orientation is equally probable), the structural complexity for both models is given by (see Appendix A for a derivation)

$$C_0 = \frac{3}{8} \left(\sum_{k=0}^{\infty} \frac{1}{4^k} \right) = \frac{3}{8} \left(\frac{4}{3} \right) = \frac{1}{2}. \quad (5)$$

On the contrary, in the ground state for the perfect classical FM and AFM orderings it suffices to analyze what happens after the first coarse-graining (CG) step, i.e., $C_0 = D_0$, since it is easy to see that all other D_k for $k > 1$ vanish:

$$\begin{bmatrix} 1 & 1 \\ 1 & 1 \end{bmatrix} \xrightarrow{\text{CG}} \begin{bmatrix} 1 & 1 \\ 1 & 1 \end{bmatrix} \rightarrow D_0 = 1 - \frac{1+1}{2} = 0 \quad (\text{FM case}), \quad (6)$$

$$\begin{bmatrix} 1 & -1 \\ -1 & 1 \end{bmatrix} \xrightarrow{\text{CG}} \begin{bmatrix} 0 & 0 \\ 0 & 0 \end{bmatrix} \rightarrow D_0 = 0 - \frac{1+0}{2} = \frac{1}{2} \quad (\text{AFM case}). \quad (7)$$

From these two limiting cases we conclude that while in the FM case C_0 must exhibit a drop from $1/2$ to 0 as one lowers the temperature and the system develops a net magnetization, in the AFM case C_0 can remain constant. We note that the variations in C_0 in Fig. 2(c) are of the order of 10^{-5} and not visible in the scale of the plot. Since the derivation at high temperatures assumes an equal number of spins up and spins down and in the perfect classical AFM ordering this balance is preserved at all temperatures, we infer that C_0 is sensitive only to the uniform magnetization of the system. As we will see later, this is also the case for the spin-balanced FHM.

On the other hand, C_1 captures the transition temperature in the AFM Ising model with great accuracy and exhibits a similar behavior to its FM counterpart: The complexity is larger in the disordered phase, but tends to zero in the ground state, illustrating that in the latter state, after a single coarse-graining step, the resulting patterns are no longer complex and there is scale invariance.

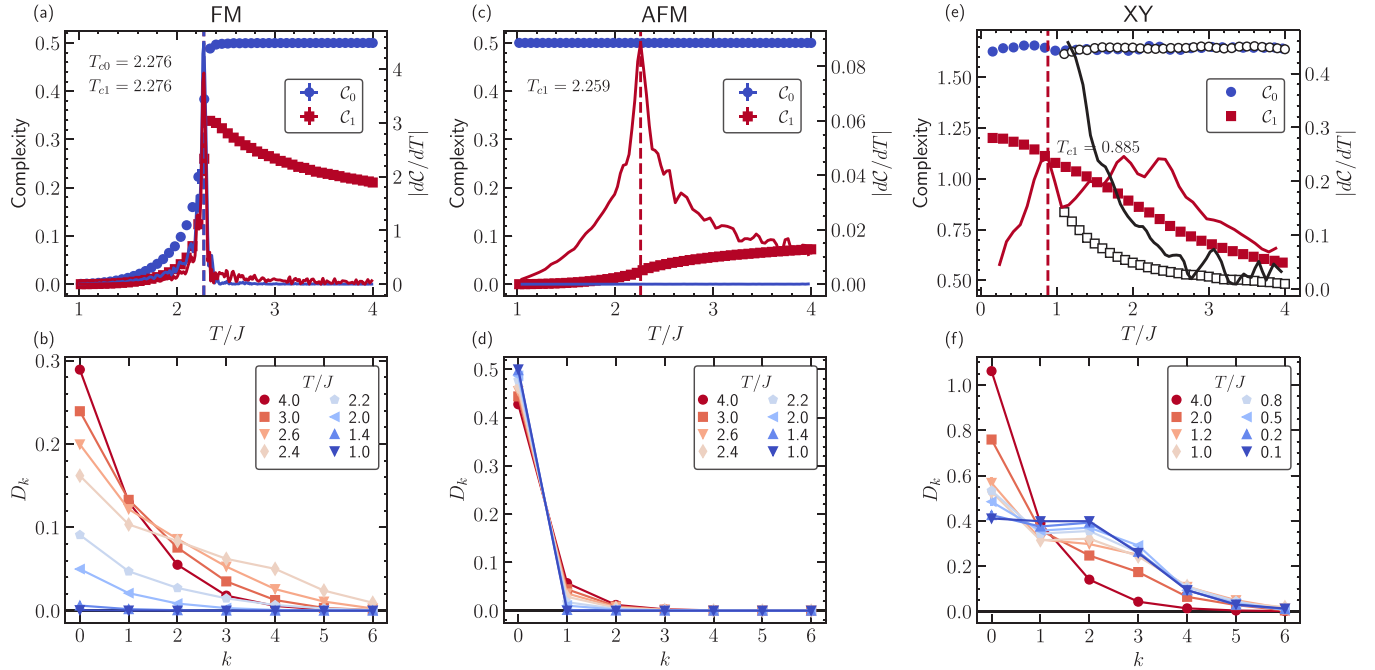


FIG. 2. Classical models in 128×128 lattices. Results are presented for Ising (a) and (b) FM and (c) and (d) AFM couplings and for (e) and (f) the XY model. (a), (c), and (e) Plots of C_0 (blue circles) and C_1 (red squares) as a function of T/J . Solid lines correspond to the absolute value of the derivative. The extracted transition temperatures T_c are consistent with the exact results in all cases. In (e) black markers and lines correspond to results obtained in 256×256 lattices. (b), (d), and (f) Plots of D_k vs k for different temperatures. The behavior of the dissimilarities for each model are significantly different.

We observe that the behaviors of the FM and AFM dissimilarities as a function of k are very different. For the AFM case [Fig. 2(d)], in the ordered phase, only D_0 is nonzero and contributions at higher k come from thermal fluctuations. Interestingly, because C_0 is constant at all T , we observe a conservation of weights in the dissimilarities. In other words, the same exact weight loss in D_k for $k > 0$ is gained by D_0 at every temperature.

Finally, we notice that D_0 in the FM Ising model closely tracks, within a prefactor, the temperature behavior of the entropy per spin S (not shown) and C_0 correlates with the Boltzmann entropy S_B , defined as [49]

$$S_B = - \sum_{\sigma} p_{\sigma} \log_2(p_{\sigma}), \quad (8)$$

where $p_{\sigma} = (1 \pm m)/2$, with m the average magnetization of the system. That means C_1 follows the trend in the “total correlation density” $\rho_c = S_B - S$ [49]. The Boltzmann entropy assumes the lack of internal correlations and corresponds to the isolated spin entropy. Since ρ_c only vanishes when no internal correlations occur, i.e., when each spin is independent, it measures how constrained the spin distribution is and is therefore maximized when the spins are strongly correlated [49].

2. Hamiltonian with $O(2)$ symmetry

We now turn our attention to the XY model. In Fig. 2(e) we show the structural complexity of the model as a function of temperature for two system sizes 128×128 (closed markers) and 256×256 (open black markers). The results are averaged

over five different initial random seeds. We further apply a moving average with a five-point window over temperature fitted with a local third-order polynomial (the Savitzky-Golay filter) to reduce noise. Similarly to the AFM Ising model, C_0 is more or less constant for all temperatures and for both system sizes, indicating the near-zero net magnetization of the system. On the contrary, C_1 increases as the temperature is lowered, indicating that the low- T phase, where the existence of pairs of vortices with opposite vorticity is expected [46], is the most complex one. We find a strong finite-size dependence in C_1 , expected to persist in this model for certain properties even with systems an order of magnitude larger in size [50]. The derivative of C_1 for the 128×128 system exhibits broad and inconclusive features at $T/J \lesssim 3$. By increasing the system size to 256×256 , these features develop into a sharp upturn at the lowest temperatures we could access in our simulations due to inflating autocorrelation times. This feature is consistent with the location of the peak in the specific heat ($T/J \sim 1.04$) and the BKT transition temperature of the model ($T_c/J = 0.894$) [50,51]. In order to access lower temperatures and larger system sizes, more sophisticated numerical algorithms are required, which are beyond the scope of this work [50,52,53].

We find that in this case, the behavior of the dissimilarities as a function of k is completely different from those for the FM or AFM Ising models as illustrated in Fig. 2(f). At high temperatures D_k decays rapidly with k . However, as the temperature is lowered, we find significant contributions to the complexity from all length scales for $T \lesssim T_c$, which we attribute to the existence of a nontrivial topological phase.

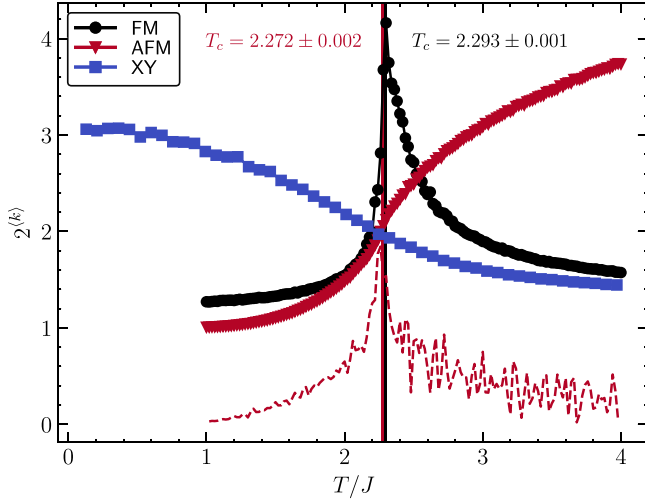


FIG. 3. Average linear length scale in the classical models. Results of $2^{(k)}$ vs T/J are shown for the classical models. We apply the linear transformation $y \rightarrow 20 \times (y - 1) + 1$ to the AFM Ising data to display their behavior on the same scale. Vertical lines indicate the location of peaks in the FM case (black) and the derivative in the AFM case (red).

3. Relevant length scales

Since the structural complexity aggregates information about correlations in the system up to a distance of Λ^k at step k , we define an average for k ,

$$\langle k \rangle = \frac{\sum_k k D_k}{\sum_k D_k} = \frac{1}{C_0} \sum_k k D_k, \quad (9)$$

and take $\Lambda^{(k)} = 2^{(k)}$ as a relevant length scale of the model. We therefore expect this quantity to reflect the cluster sizes needed to describe the behavior of the system at different temperatures.

We show $2^{(k)}$ vs T/J in Fig. 3 for the classical models considered here. In the case of the FM Ising model, it grows rapidly near T_c as the temperature is lowered and then rapidly falls in the ordered phase. Its behavior is reminiscent of the critical behavior of the magnetic susceptibility of the model. The location of the peak in this quantity (black vertical line in Fig. 3) provides a great estimate for T_c . Interestingly, we find that the behavior of $2^{(k)}$ for the AFM Ising model resembles the shape of the energy and its derivative (red dashed line in Fig. 3) predicts an accurate estimate for T_c too (its peak location is denoted by the red vertical line). Finally, for the XY model, $2^{(k)}$ grows as the temperature is lowered, indicating a growing length scale for relevant correlations, consistent with the nontrivial topological order the system exhibits.

B. Fermi-Hubbard model

In Fig. 4 we present examples of the simulated snapshots of n_σ , m_z , and n for $U/t = 8$, three different filling fractions ($\delta = 0, 0.18, 0.5$), and three temperatures ($T/t = 5, 1, 0.4$). In the half-filled case, where there is on average one particle per site (top row), as the temperature is lowered, one can observe signatures of (i) Mott physics (formation of more uniform local moments), (ii) antiferromagnetism (checkerboard patterns in the n_σ snapshots), and (iii) superexchange physics, i.e., doublon-hole quantum fluctuations which occur at neighboring sites in the n snapshots and are necessary for antiferromagnetism to emerge [25]. In contrast, results at 18% doping (middle row) exhibit remnants of the parent AFM state, but the presence and behavior of holes is more complicated. Finally, at 50% doping (bottom row) in the Fermi liquid regime, electrons tend to avoid each other (Pauli hole) and, other than the reduction in double occupancies, there do not seem to be any significant changes as the temperature is lowered.

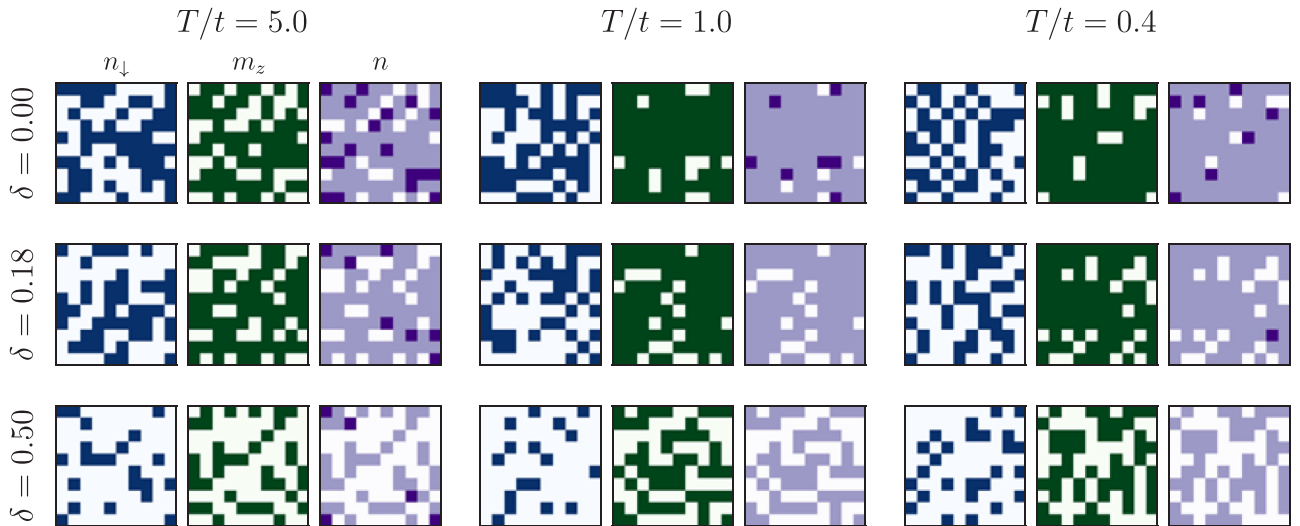


FIG. 4. Sample simulated snapshots of the FHM at $U/t = 8$ in 10×10 lattices. Results are presented at densities $\langle n \rangle = 1, 0.82, 0.5$ for temperatures $T/t = 5, 1, 0.4$ for n_\downarrow densities (blue), the local moment $m_z = |n_\uparrow - n_\downarrow|$ (green), and total density $n = n_\uparrow + n_\downarrow$ (purple). White corresponds to 0; blue, green, and light purple to 1; and dark purple to 2.

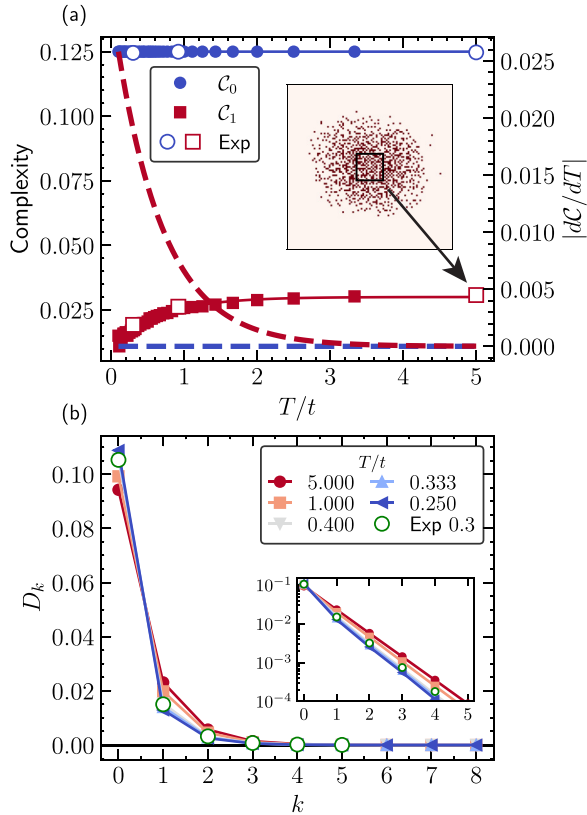


FIG. 5. Structural complexity and dissimilarities of the half-filled FHM at $U/t = 8$ from spin-resolved snapshots. (a) Plot of C_0 (blue circles) and C_1 (red squares) from 10×10 simulated snapshots as a function of temperature. Dashed lines are derivatives and open markers are based on experimental data. The inset is an example of the experimental snapshots and the 16×16 region used for the analysis. (b) Dissimilarities as a function of coarse-graining steps at different temperatures. Experimental data at $T/t = 0.3$ are shown as open green circles. The inset shows the same data in logarithmic scale.

1. Spin-resolved densities n_σ

In Fig. 5(a) we show the structural complexity of single-species snapshots of the half-filled FHM as a function of temperature. We observe that C_0 is constant for all temperatures, similar to what was observed in the AFM Ising model, indicating a spin-balanced mixture. On the contrary, C_1 decays monotonically as the temperature is lowered. Its derivative (red dashed line) appears to diverge as $T \rightarrow 0$, in agreement with the fact that for the 2D FHM, the Néel transition occurs at $T_N = 0$.

Results for the corresponding dissimilarities as a function of the coarse-graining step at different temperatures exhibit behavior similar to that for the AFM Ising model [see Fig. 5(b)]. More specifically, the weight lost by D_0 as the temperature increases is gained by $D_{k>0}$. There is however a fundamental difference here corresponding to the nonvanishing D_1 at all temperatures, which signals the presence of quantum fluctuations in the model. The C_0 is constant despite that.

For both the complexities and the dissimilarities, results based on snapshots that are obtained experimentally using a quantum gas microscope [36] (denoted by open markers) are

in excellent agreement with the theory curves. Furthermore, this agreement between the numerical and experimental values of the dissimilarities holds for every D_k at all temperatures considered, as evidenced in Fig. 6 where we show D_k vs T/t for the half-filled case and the 18% doped FHM. Such excellent agreement demonstrates the applicability of the method to current experiments involving ultracold atoms in optical lattices.

More interestingly, we find that C_1 vs temperature or doping exhibits the same trends as the entropy per site S/N in the model (see Fig. 7 for the doping dependence at different temperatures). We observe that below $T/t < 1$, the structural complexity develops a peak around 20% doping. Although the peak in the entropy occurs at a slightly lower doping (see the inset of Fig. 7), the shape and trends are fairly similar. Additionally, we also observe good agreement with the experimental data at all temperatures considered, which further supports the validity of our results. Because of the correlation between C_1 and S/N , this suggests the structural complexity of Fermi-Hubbard snapshots can be used as a quick and rapid proxy for the entropy of the system. This can be very useful in optical lattice experiments, where after loading the lattice, the calculation of the entropy is not straightforward [55].

It is worth mentioning that previous studies in one-dimensional systems, bit strings [40] and the extended Hubbard model [42], have demonstrated that the structural complexity draws a close analog to the entanglement entropy since both capture the existence of nonlocal correlations in the models. In the present study we do not have access to the entanglement entropy and therefore only focus on the thermodynamic entropy. Although the entanglement entropy and the thermodynamic entropy are not equivalent to each other, they are associated with the development of correlations in the system and with the freezing of degrees of freedom, respectively, which generally occur together as we vary a tuning parameter. The establishment of connections between the structural complexity and the entanglement entropy in doped Fermi-Hubbard models at finite T is an open question that requires further exploration.

Another important observation is the fact that at the temperatures considered, the region where the structural complexity is maximal corresponds to the strange metal region. The broad peak in C_1 spanning $\delta \in [10\%, 30\%]$ is consistent with the doping value $\delta_c \sim 30\%$ that corresponds to the crossover to the Fermi liquid phase [56]. Moreover, the trends in the structural complexity vs doping illustrate that features related to phases that emerge in this doping range at lower temperatures (such as fluctuating stripes [30–32]) are more complex than the AFM parent state at half filling and that this metallic region is also more complex than the conventional Fermi liquid found at larger dopings. As optical lattice experiments evolve and stripe physics becomes available, we expect that signatures of the presence and periodicity of stripe orderings should be detectable by analyzing the contributions of the dissimilarities at different scales and C_1 .

2. Local moments and total density

Before quantum gas microscopy had access to images of both fermionic species of the same system at the same time,

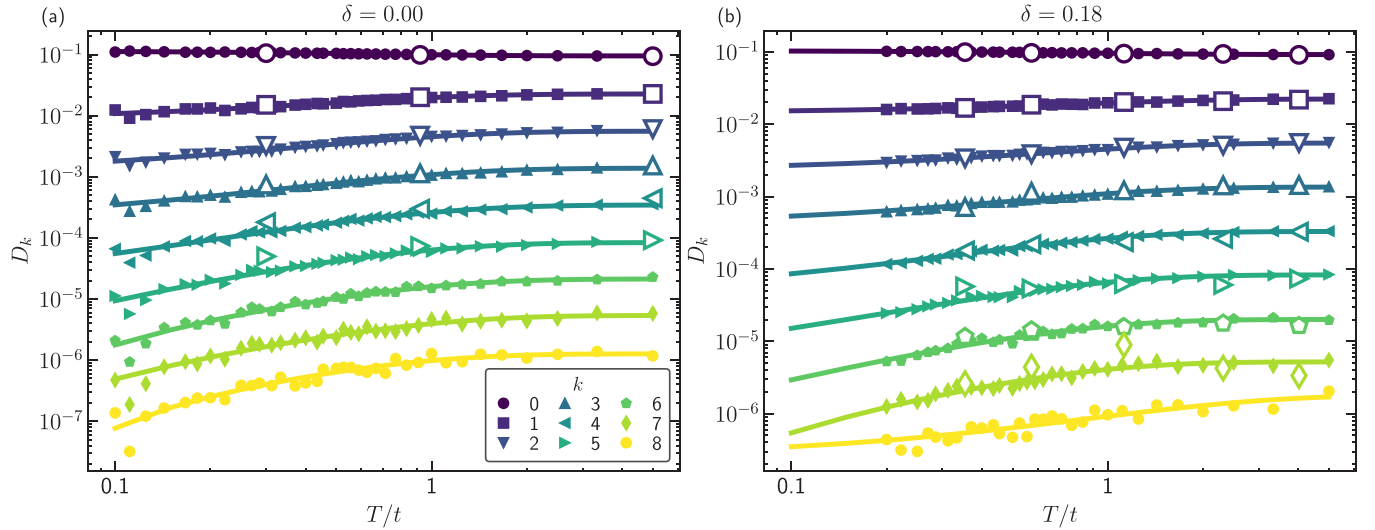


FIG. 6. Dissimilarities D_k in the FHM at $U/t = 8$ from spin-resolved snapshots for (a) $\delta = 0$ and (b) $\delta = 0.18$. Closed markers correspond to simulated snapshots in 10×10 lattices and open markers to experimental data. Solid lines are exponential fits to the data. In both cases, D_k exhibits an exponential decay with temperature (solid lines) and a rapid suppression with increasing k .

density snapshots of the FHM could not be obtained; only local moments could be detected separately. Nowadays, with spin-resolved imaging, local moments as well as total density images can be created [27,28,57]. In this section we study their structural complexities and dissimilarities.

In Fig. 8(a) we show the structural complexities of the local moments (open markers and dashed lines) and the total density (closed markers and solid lines) of the half-filled FHM as a function of temperature. In contrast to what we observed for the spin-resolved snapshots, C_0 is not constant but exhibits a nonmonotonic behavior as a function of T/t . This is because unlike for single-species snapshots, as the temperature changes, the number of doublons, and therefore the balance

between filled and empty pixels in the snapshots, changes too. Such nonmonotonic behavior persists for C_1 , albeit with smaller magnitude changes.

We find that for $T/t \leq 2$, C_0 for the density snapshots is larger than for the local moment snapshots, but the opposite is true for C_1 . We can understand this through the following argument: Below the characteristic AFM temperature, where the upturn in double occupancy starts as we lower T , for density snapshots, the doublon-hole fluctuations take place on nearest-neighbor sites and so the first coarse-graining step already renders mostly uniform images. On the contrary, for local moment snapshots, because both holes and doublons show up as empty pixels, one still has significant structure for later coarse-graining steps.

To complement these results, in Fig. 8(b) we show the dissimilarities of the half-filled FHM as a function of coarse-graining steps at different temperatures. The D_k for both the local moments and total density exhibit an exponential decay with k at fixed T/t .

In Fig. 9, we show the temperature dependence of the dissimilarities for the density snapshots at $\delta = 0.18$. Here we observe that (i) D_k decays rapidly with increasing k , (ii) D_0 exhibits a nonmonotonic behavior with T/t , akin to the double occupancy, $\mathcal{D} = \langle n_{i\uparrow} n_{i\downarrow} \rangle$, and (iii) it closely follows the function $\mathcal{D}' = (3/4)[\mathcal{D} + 0.5\delta(1 - \delta)]$. This expression can be derived analytically under the assumption that the uncorrelated parts of the correlation functions dominate (see Appendix B), and it holds for other dopings too. The agreement at high T , where the assumption is valid, illustrates that D_0 for the density snapshots is in fact closely related to the double occupancy fraction in the model. More important are the discrepancies at $T/t \leq 1$, which signal the presence of nontrivial two-point nearest- and next-nearest-neighbor spin-resolved density-density correlations in the model. A similar approximation for D_0 based on local moment snapshots proves challenging as three-point and four-point density correlators enter the analysis (see Appendix B).

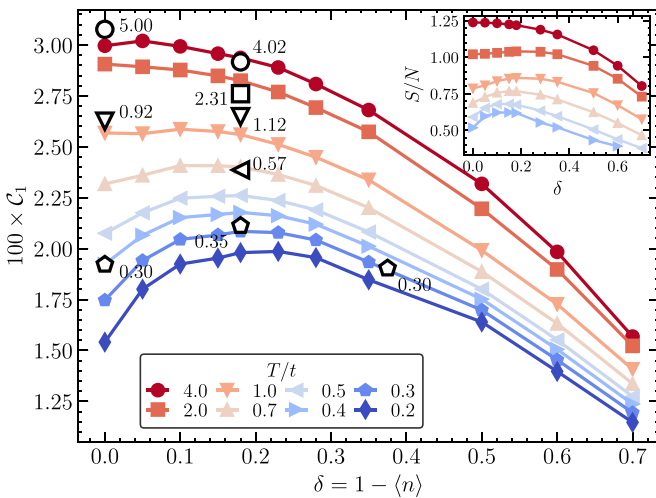


FIG. 7. Plot of C_1 vs δ for the FHM at $U/t = 8$ from spin-resolved snapshots. Closed markers correspond to simulated snapshots and open black markers to experimental data. Temperature estimates from the experiment are indicated next to each marker. The inset shows the entropy per site as a function of doping from the numerical linked-cluster expansion (NLCE) [54].

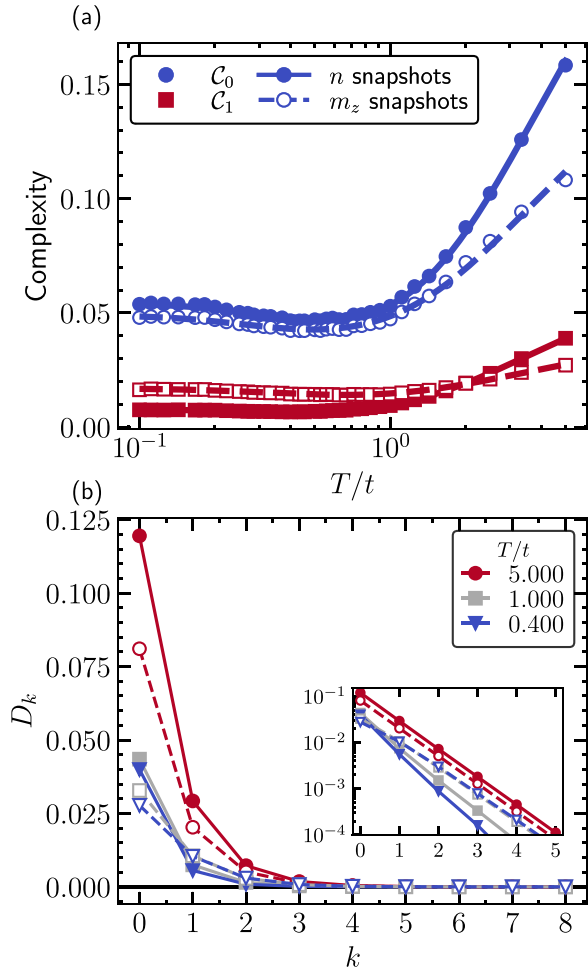


FIG. 8. Structural complexity of the half-filled FHM at $U/t = 8$ from simulated density and local moment snapshots. (a) Plot of C_0 (blue circles) and C_1 (red squares) as a function of temperature for the local moments (open markers) and the total density (solid markers). Lines are guides to the eye. (b) Dissimilarities as a function of coarse-graining steps at different temperatures for local moments (open markers) and total density (solid markers). The inset presents the same data in logarithmic scale.

Figure 10(a) shows C_0 as a function of δ for the density snapshots along with a shifted \mathcal{D} from the numerical linked-cluster expansion [54,58,59] for each value of the doping. Here C_0 exhibits an interesting behavior: (i) It is nonmonotonic with temperature for all values of δ , (ii) it is largest at $\delta = 0.5$, except at very high temperatures, and remarkably (iii) it fully matches the shifted double occupancies at all temperatures and all dopings considered. Previously, we discussed that D_0 is closely correlated to the double occupancy fraction in the model. When higher-order D_k 's are added, they capture the remaining features of the double occupancy and therefore C_0 captures its temperature dependence extremely well.

In contrast, the structural complexities of the local moment snapshots [Fig. 10(b)] are more complicated to interpret. Although the behaviors of the curves for all dopings except $\delta = 0.5$ look fairly similar to their counterparts based on density, we are unable to derive a simple analytic expression

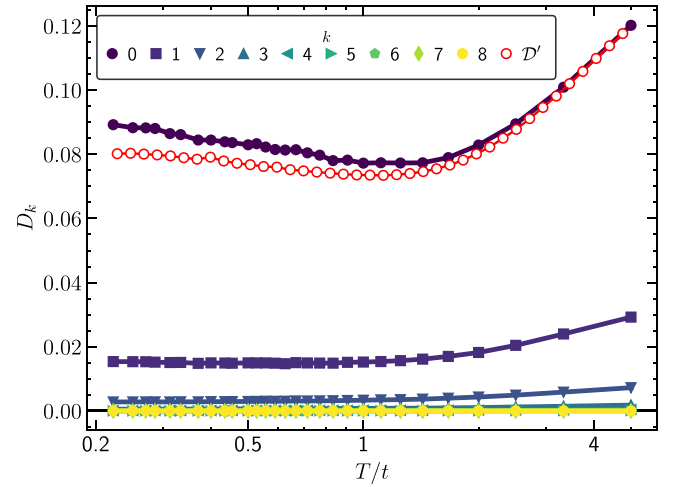


FIG. 9. Plot of D_k vs T/t for the FHM with $U/t = 8$ from simulated density snapshots at 18% doping for $\delta = 0.18$. Red open markers come from the NLCE for $\mathcal{D}' = (3/4)[\mathcal{D} + 0.5\delta(1 - \delta)]$.

based on thermodynamic properties in this case due to the presence of higher-order correlations even at the first coarse-graining step. The most interesting region for this complexity occurs at $\delta = 0.5$, where, for $T/t \leq 1$, $C_0 = 0.125$, the same constant value of the structural complexity as for the single-species snapshots at half filling. This region corresponds to the charge-density wave phase observed at quarter filling in the FHM [25,36], where one sublattice is occupied and other sublattice is empty, and therefore C_0 is merely capturing the classical complexity associated with having the largest entropy in the images with an equal number of empty and filled pixels.

Contrary to what occurred with the single-species snapshots, here we do not find excellent agreement between experiment and theory. Figure 10(b) displays experimental data at different dopings as open markers. For $\delta = 0.35$ the open diamond indeed matches with the simulations at the same doping. However, C_0 at $\delta = 0.6$ has the same value. On the other hand, for data at $\delta = 0.18$, the open left triangles match fairly well with the simulations at a slightly larger doping of $\delta = 0.23$, which might suggest the experimental data were taken at such higher doping. Finally, C_0 based on experimental data at half filling does not show good agreement with that calculated for the simulated images and therefore could signal issues with the imaging procedure. Hence, the structural complexity of local moments can be used to further diagnose imaging issues.

Figure 11 presents $2^{(k)}$ vs doping at different temperatures for the three different types of snapshots analyzed. At the highest temperature considered, $T/t = 4$, $2^{(k)}$ increases slowly with δ for the n_σ and n snapshots, but decreases for the m_z snapshots. This trend persists down to all temperatures considered for the m_z snapshots, becoming sharper as the temperature is lowered, but surprisingly exhibiting a crossing at $\delta \sim 18\%$, which points to a possible temperature-independent length scale in m_z at this doping. This coincides with the region where structural complexity is maximal and corresponds to the strange metal region.

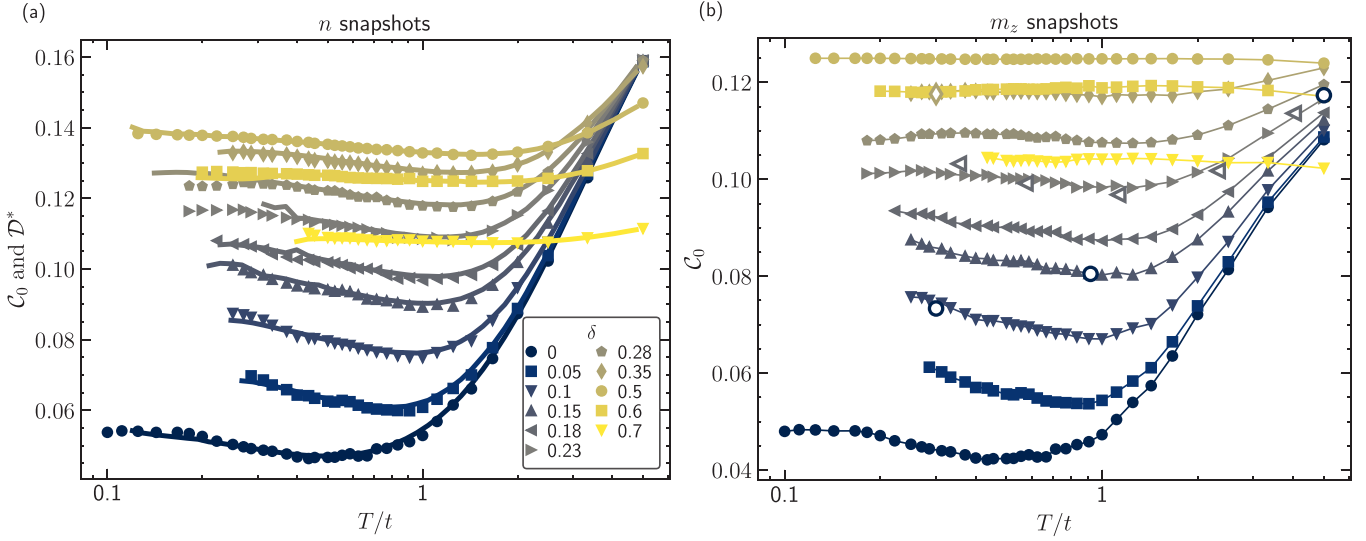


FIG. 10. Plot of C_0 vs T/t for the FHM at $U/t = 8$ from density and local moment snapshots. (a) Total density n . Markers correspond to the structural complexity and lines to $D^* = D + 0.5\delta(1 - \delta)$ obtained with NLCE. (b) Local moments m_z . Closed markers are based on simulated snapshots, open markers are based on experimental ones, and lines are guides to the eye.

Since this occurs at easily experimentally-accessible regimes, it is a phenomenon that can be explored immediately in the experiment.

The plot of $2^{(k)}$ vs temperature for n_σ and n snapshots also displays interesting behaviors at the same doping. As seen in Fig. 11(a) for n_σ , the curves develop a plateau that starts around $\delta \sim 18\%$ and extends up to $\delta \sim 40\%$, while for n in Fig. 11(b) the curves develop a broad peak around $\delta \sim 18\%$.

IV. CONCLUSION

In this paper we showed how the structural complexity, derived from overlaps of consecutive coarse grainings of images, can be used to analyze real-space snapshots of strongly correlated electronic systems to reveal their underlying physics. We benchmarked our results for classical models of magnetism and showed that the complexity measure can predict the magnetic moment and the critical temperature very well. We then turned to the FHM and computed the structural complexity for various types of snapshots generated via DQMC simulations or obtained through quantum gas microscopy in

optical lattice experiments. Among other things, we found that when calculated for the total density snapshots, it matches the double occupancy as a function of temperature shifted by a density-dependent term. We identified specific contributions that correlate with the entropy of the system as a function of doping when dealing with snapshots of individual species of fermions. Dissimilarities of patterns at different coarse-graining steps also revealed relevant length scales in different regions and pointed to interesting behaviors near 18%, where the strange metal phase was observed. Hence, the technique promises a theory-free method to extract phase changes or even physical properties not otherwise accessible based on experimental images alone. To that end, we have developed an open-source PYTHON package [60].

An immediate application of this technique can be for the study of Fermi-Hubbard models with larger spins and enhanced $SU(N > 2)$ symmetries, which are expected to exhibit exotic behaviors with a complicated N dependence [61–65]. In recent years, experiments with alkaline-earth-like atoms in optical lattices have studied the $SU(N)$ FHM [66–71], and future implementations of quantum gas mi-

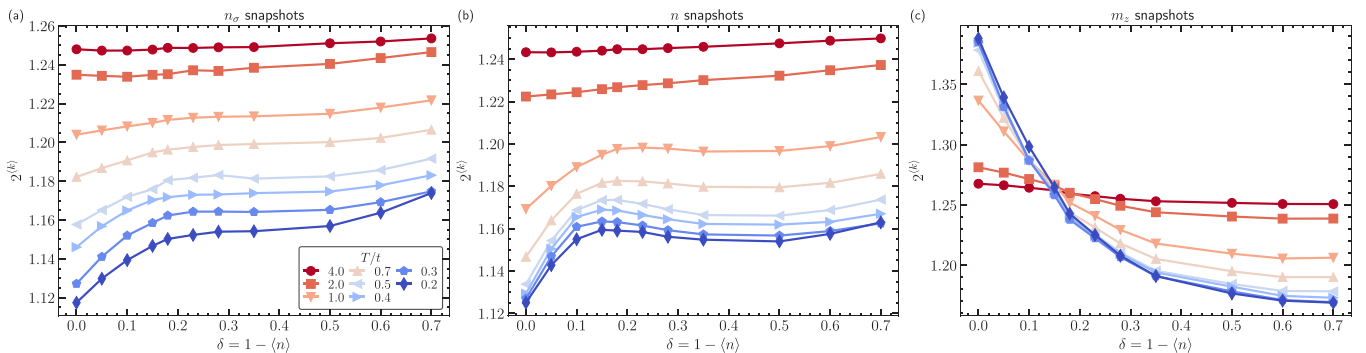


FIG. 11. Average linear length scale obtained from dissimilarities vs doping from (a) single-species n_σ , (b) total density n , and (c) local moment m_z snapshots.

croscopes for two-dimensional optical lattices will provide spin-resolved projective measurements of the $SU(N)$ FHM, which can be analyzed using the multiscale structural complexity to extract valuable physics. Furthermore, we expect the technique to also be useful to analyze other types of ultracold-atom experiments images, such as absorption imaging of interferometric patterns [72,73] and self-similarities of atomic wave packets [74].

In addition, future work will explore the possibility of extending the structural complexity measure to other lattice geometries. This is motivated by the field's interest in studying frustration in triangular [14–17] and kagome [75] lattices with ultracold atoms, as well as the exotic physics that arises due to the nonperiodicity in quasicrystals [76], and the flexibility of engineering arbitrary lattice geometries using optical tweezer arrays [77,78].

A particularly intriguing application would be to employ the structural complexity to study time-independent and time-dependent Green's functions, since the dynamical properties of models used to describe strongly interacting matter such as the Hubbard, Holstein, and Su-Schrieffer-Heeger Hamiltonians are much more challenging to explore using conventional numerical approaches.

ACKNOWLEDGMENTS

We are grateful to Waseem Bakr, Elmer Guardado-Sanchez, and Benjamin M. Spar for sharing their experimental snapshots for the Fermi-Hubbard model with us. We also thank Waseem Bakr and Martin Zwierlein for their useful comments on our manuscript. The authors were supported by Grant No. DE-SC-0022311, funded by the U.S. Department of Energy, Office of Science. E.I.-G.-P. would like to acknowledge useful discussions with Steven Johnston and Benjamin Cohen-Stead while visiting the University of Tennessee, Knoxville.

APPENDIX A: EXPRESSION FOR C_0 IN THE INFINITE-TEMPERATURE LIMIT

In this Appendix we derive the structural complexity for the Ising models in the fully disordered phase, i.e., where each spin orientation is equally probable, given by Eq. (5).

Let us calculate D_0 first. For the 2×2 coarse-graining window, we have $2^4 = 16$ equally probable combinations of 1's and -1 's. After the first coarse-graining step, the coarse-grained values obey a binomial distribution. These are

TABLE I. Possible values for the first coarse-graining step and associated probabilities, as well as the values and probabilities of the overlaps for the fully disordered spin snapshots.

Coarse-grained step		Overlaps	
Value	Probability	Value	Probability
± 1	1/16	0	1/8
$\pm 1/2$	1/4	3/8	1/2
0	1/8	1/2	3/8

TABLE II. Possible values for the second coarse-graining step and associated probabilities, as well as the values and probabilities of the overlaps for the fully disordered spin snapshots.

Coarse-grained step		Overlaps	
Value	Probability	Value	Probability
± 1	1/65536	0	905/32768
$\pm 7/8$	1/4096	3/128	329/2048
$\pm 3/4$	15/8192	1/32	111/1024
$\pm 5/8$	35/4096	1/16	9/64
$\pm 1/2$	455/16384	11/128	207/1024
$\pm 3/8$	273/4096	3/32	239/4096
$\pm 1/4$	1001/8192	1/8	123/4096
$\pm 1/8$	715/4096	19/128	39/512
0	6435/32768	5/32	9/128
		3/16	21/512
		27/128	83/2048
		1/4	27/4096
		35/128	9/512
		9/32	9/1024
		5/16	3/512
		43/128	3/2048
		11/32	9/4096
		3/8	1/8192
		51/128	3/2048
		1/2	3/32768

presented in Table I, as well as the values and probabilities of the overlaps $|O_{1,0} - \frac{1}{2}(O_{1,1} + O_{0,0})|$.

With these results we can calculate the average $D_0 = \sum_n p_n d_n$, where d_n corresponds to the value of the overlap and p_n its probability. In this case,

$$D_0 = (0 \times \frac{1}{8}) + (\frac{1}{2} \times \frac{3}{8}) + (\frac{3}{8} \times \frac{1}{2}) = \frac{3}{8}. \quad (\text{A1})$$

In order to calculate D_1 , we now have to consider $5^4 = 625$ possible combinations for each window. After the second coarse-graining step, the values and overlaps obey the probabilities presented in Table II.

With these results we calculate the average D_1 as

$$D_1 = \frac{3}{32} = D_0 \times (\frac{1}{4}). \quad (\text{A2})$$

It is then easy to prove that the next dissimilarities involved in computing the structural complexity are given by

$$D_k = D_0 \times \left(\frac{1}{4^k}\right), \quad (\text{A3})$$

and therefore we arrive at Eq. (5).

APPENDIX B: EXPRESSIONS FOR D_0 FOR THE DENSITY AND LOCAL MOMENT SNAPSHOTS

To simplify reading the following equations, in this Appendix we use two indices ij to label a site in an image.

Now let us consider a two-dimensional image with linear dimension L and $N = L \times L$ sites. On each site, given by the coordinate pair ij , the value of the image is u_{ij} . The first term

D_0 is given by

$$D_0 = \frac{1}{4N} \left| \sum_{i,j=1}^{L/2} [u_{2i-1,2j-1}(u_{2i-1,2j} + u_{2i,2j-1}) + u_{2i,2j-1}(u_{2i-1,2j} + u_{2i,2j}) + u_{2i,2j}(u_{2i-1,2j-1} + u_{2i-1,2j})] - \frac{3}{2} \sum_{i,j=1}^L u_{ij}^2 \right| \quad (\text{B1})$$

and it captures all correlations within a unit window, i.e., on-site nearest and next-nearest neighbors.

In the case of density snapshots the images correspond to $u_{ij} = n_{ij,\uparrow} + n_{ij,\downarrow}$. So D_0 is given by

$$D_0 = \frac{1}{4N} \left| 2(\langle n_{\uparrow} n_{\uparrow} \rangle_{nm} + \langle n_{\uparrow} n_{\downarrow} \rangle_{nm}) + (\langle n_{\uparrow} n_{\uparrow} \rangle_{nmn} + \langle n_{\uparrow} n_{\downarrow} \rangle_{nmn}) - \frac{3}{2} \rho - 3\mathcal{D} \right|, \quad (\text{B2})$$

where we exploited the translational and rotational symmetry and $\langle n_{\sigma} n_{\tau} \rangle_{nm}$ is shorthand for nearest-neighbor density-density correlations for spin σ and τ . The subindex nmn indicates the next-nearest-neighbor correlator. When the un-

correlated part of these correlation functions dominates (for example, at high T), $\langle n_{\uparrow} n_{\uparrow} \rangle_{nm} = \langle n_{\uparrow} n_{\downarrow} \rangle_{nm} = \langle n_{\uparrow} n_{\uparrow} \rangle_{nmn} = \langle n_{\uparrow} n_{\downarrow} \rangle_{nmn} = \rho^2/4$ and so

$$D_0 \approx \frac{1}{4} \left| \frac{3}{2} \rho^2 - \frac{3}{2} \rho - 3\mathcal{D} \right| = \frac{3}{4} \left| \frac{1}{2} \delta(1 - \delta) - \mathcal{D} \right|. \quad (\text{B3})$$

This final expression indicates that the double occupancy, shifted by an amount $0.5\delta(1 - \delta)$ and rescaled, should agree with D_0 .

In the case of the local moments, the images correspond to $u_{ij} = (n_{ij,\uparrow} - n_{ij,\downarrow})^2$. Working out the expressions and under the same assumptions of translational, rotational, spin permutation symmetry, and that the correlated part of the functions dominate, we find

$$D_0 \approx \frac{1}{4} \left| \frac{3}{2} \frac{1}{4} \rho^2 (2 - \rho^2) - \frac{3}{2} m_z \right| = \frac{3}{8} \left| \frac{1}{4} (1 - \delta^2)^2 - m_z \right|. \quad (\text{B4})$$

We expect that the disagreement between this D_0 and any simple function of m_z is related to the fact that three-point and four-point density correlators enter the analysis, i.e., the assumption that the uncorrelated parts dominate is no longer valid.

-
- [1] S. R. White, D. J. Scalapino, R. L. Sugar, E. Y. Loh, J. E. Gubernatis, and R. T. Scalettar, Numerical study of the two-dimensional Hubbard model, *Phys. Rev. B* **40**, 506 (1989).
- [2] D. Scalapino, Superconductivity and spin fluctuations, *J. Low Temp. Phys.* **117**, 179 (1999).
- [3] T. A. Maier, M. S. Jarrell, and D. J. Scalapino, Structure of the pairing interaction in the two-dimensional Hubbard model, *Phys. Rev. Lett.* **96**, 047005 (2006).
- [4] D. P. Arovas, E. Berg, S. Kivelson, and S. Raghu, The Hubbard model, *Annu. Rev. Condens. Matter Phys.* **13**, 239 (2022).
- [5] M. Qin, C.-M. Chung, H. Shi, E. Vitali, C. Hubig, U. Schollwöck, S. R. White, and S. Zhang (Simons Collaboration on the Many-Electron Problem), Absence of superconductivity in the pure two-dimensional Hubbard model, *Phys. Rev. X* **10**, 031016 (2020).
- [6] M. Qin, T. Schäfer, S. Andergassen, P. Corboz, and E. Gull, The Hubbard model: A computational perspective, *Annu. Rev. Condens. Matter Phys.* **13**, 275 (2022).
- [7] R. Jördens, L. Tarruell, D. Greif, T. Uehlinger, N. Strohmaier, H. Moritz, T. Esslinger, L. De Leo, C. Kollath, A. Georges *et al.*, Quantitative determination of temperature in the approach to magnetic order of ultracold fermions in an optical lattice, *Phys. Rev. Lett.* **104**, 180401 (2010).
- [8] T. Paiva, R. Scalettar, M. Randeria, and N. Trivedi, Fermions in 2D optical lattices: Temperature and entropy scales for observing antiferromagnetism and superfluidity, *Phys. Rev. Lett.* **104**, 066406 (2010).
- [9] U. Schneider, L. Hackermüller, J. P. Ronzheimer, S. Will, S. Braun, T. Best, I. Bloch, E. Demler, S. Mandt, D. Rasch, and A. Rosch, Fermionic transport and out-of-equilibrium dynamics in a homogeneous Hubbard model with ultracold atoms, *Nat. Phys.* **8**, 213 (2012).
- [10] D. Greif, T. Uehlinger, G. Jotzu, L. Tarruell, and T. Esslinger, Short-range quantum magnetism of ultracold fermions in an optical lattice, *Science* **340**, 1307 (2013).
- [11] R. A. Hart, P. M. Duarte, T.-L. Yang, X. Liu, T. Paiva, E. Khatami, R. T. Scalettar, N. Trivedi, D. A. Huse, and R. G. Hulet, Observation of antiferromagnetic correlations in the Hubbard model with ultracold atoms, *Nature (London)* **519**, 211 (2015).
- [12] M. Boll, T. A. Hilker, G. Salomon, A. Omran, J. Nespolo, L. Pollet, I. Bloch, and C. Gross, Spin-and density-resolved microscopy of antiferromagnetic correlations in Fermi-Hubbard chains, *Science* **353**, 1257 (2016).
- [13] A. Mazurenko, C. S. Chiu, G. Ji, M. F. Parsons, M. Kanász-Nagy, R. Schmidt, F. Grusdt, E. Demler, D. Greif, and M. Greiner, A cold-atom Fermi-Hubbard antiferromagnet, *Nature (London)* **545**, 462 (2017).
- [14] M. Xu, L. H. Kendrick, A. Kale, Y. Gang, G. Ji, R. T. Scalettar, M. Lebrat, and M. Greiner, Frustration-and doping-induced magnetism in a Fermi-Hubbard simulator, *Nature (London)* **620**, 971 (2023).
- [15] J. Mongkolkiattichai, L. Liu, D. Garwood, J. Yang, and P. Schauss, Quantum gas microscopy of a geometrically frustrated Hubbard system, *Phys. Rev. A* **108**, L061301 (2023).
- [16] M. Lebrat, M. Xu, L. H. Kendrick, A. Kale, Y. Gang, P. Seetharaman, I. Morera, E. Khatami, E. Demler, and M. Greiner, Observation of Nagaoka polarons in a Fermi-Hubbard quantum simulator, [arXiv:2308.12269](https://arxiv.org/abs/2308.12269).
- [17] M. L. Prichard, B. M. Spar, I. Morera, E. Demler, Z. Z. Yan, and W. S. Bakr, Directly imaging spin polarons in a kinetically frustrated Hubbard system, [arXiv:2308.12951](https://arxiv.org/abs/2308.12951).
- [18] W. S. Bakr, J. I. Gillen, A. Peng, S. Fölling, and M. Greiner, A quantum gas microscope for detecting single atoms in

- a Hubbard-regime optical lattice, *Nature (London)* **462**, 74 (2009).
- [19] L. W. Cheuk, M. A. Nichols, M. Okan, T. Gersdorf, V. V. Ramasesh, W. S. Bakr, T. Lompe, and M. W. Zwierlein, Quantum-gas microscope for fermionic atoms, *Phys. Rev. Lett.* **114**, 193001 (2015).
- [20] M. F. Parsons, A. Mazurenko, C. S. Chiu, G. Ji, D. Greif, and M. Greiner, Site-resolved measurement of the spin-correlation function in the Fermi-Hubbard model, *Science* **353**, 1253 (2016).
- [21] S. A. Moses, J. P. Covey, M. T. Miecniowski, D. S. Jin, and J. Ye, New frontiers for quantum gases of polar molecules, *Nat. Phys.* **13**, 13 (2017).
- [22] E. Altman, K. R. Brown, G. Carleo, L. D. Carr, E. Demler, C. Chin, B. DeMarco, S. E. Economou, M. A. Eriksson, K.-M. C. Fu, M. Greiner, K. R. A. Hazzard, R. G. Hulet, A. J. Kollár, B. L. Lev, M. D. Lukin, R. Ma, X. Mi, S. Misra, C. Monroe *et al.*, Quantum simulators: Architectures and opportunities, *PRX Quantum* **2**, 017003 (2021).
- [23] C. Gross and I. Bloch, Quantum simulations with ultracold atoms in optical lattices, *Science* **357**, 995 (2017).
- [24] I. Bloch, J. Dalibard, and S. Nascimbène, Quantum simulations with ultracold quantum gases, *Nat. Phys.* **8**, 267 (2012).
- [25] L. W. Cheuk, M. A. Nichols, K. R. Lawrence, M. Okan, H. Zhang, E. Khatami, N. Trivedi, T. Paiva, M. Rigol, and M. W. Zwierlein, Observation of spatial charge and spin correlations in the 2D Fermi-Hubbard model, *Science* **353**, 1260 (2016).
- [26] C. Gross and W. S. Bakr, Quantum gas microscopy for single atom and spin detection, *Nat. Phys.* **17**, 1316 (2021).
- [27] T. Hartke, B. Oreg, N. Jia, and M. Zwierlein, Doublon-hole correlations and fluctuation thermometry in a Fermi-Hubbard gas, *Phys. Rev. Lett.* **125**, 113601 (2020).
- [28] T. Hartke, B. Oreg, C. Turnbaugh, N. Jia, and M. Zwierlein, Direct observation of nonlocal fermion pairing in an attractive Fermi-Hubbard gas, *Science* **381**, 82 (2023).
- [29] A. Bohrdt, L. Homeier, C. Reinmoser, E. Demler, and F. Grusdt, Exploration of doped quantum magnets with ultracold atoms, *Ann. Phys. (NY)* **435**, 168651 (2021).
- [30] E. W. Huang, C. B. Mendl, H.-C. Jiang, B. Moritz, and T. P. Devereaux, Stripe order from the perspective of the Hubbard model, *npj Quantum Mater.* **3**, 22 (2018).
- [31] P. Mai, N. S. Nichols, S. Karakuzu, F. Bao, A. D. Maestro, T. A. Maier, and S. Johnston, Robust charge-density-wave correlations in the electron-doped single-band Hubbard model, *Nat. Commun.* **14**, 2889 (2023).
- [32] E. W. Huang, T. Liu, W. O. Wang, H.-C. Jiang, P. Mai, T. A. Maier, S. Johnston, B. Moritz, and T. P. Devereaux, Fluctuating intertwined stripes in the strange metal regime of the Hubbard model, *Phys. Rev. B* **107**, 085126 (2023).
- [33] B. Xiao, Y.-Y. He, A. Georges, and S. Zhang, Temperature dependence of spin and charge orders in the doped two-dimensional Hubbard model, *Phys. Rev. X* **13**, 011007 (2023).
- [34] S. Johnston, E. Khatami, and R. Scalettar, A perspective on machine learning and data science for strongly correlated electron problems, *Carbon Trends* **9**, 100231 (2022).
- [35] A. Bohrdt, C. S. Chiu, G. Ji, M. Xu, D. Greif, M. Greiner, E. Demler, F. Grusdt, and M. Knap, Classifying snapshots of the doped Hubbard model with machine learning, *Nat. Phys.* **15**, 921 (2019).
- [36] E. Khatami, E. Guardado-Sanchez, B. M. Spar, J. F. Carrasquilla, W. S. Bakr, and R. T. Scalettar, Visualizing strange metallic correlations in the two-dimensional Fermi-Hubbard model with artificial intelligence, *Phys. Rev. A* **102**, 033326 (2020).
- [37] S. Striegel, E. Ibarra-García-Padilla, and E. Khatami, Machine learning detection of correlations in snapshots of ultracold atoms in optical lattices, *arXiv:2310.03267*.
- [38] J. Nelson, R. Tiwari, and S. Sanvito, Machine learning density functional theory for the Hubbard model, *Phys. Rev. B* **99**, 075132 (2019).
- [39] A. A. Bagrov, I. A. Iakovlev, A. A. Iliasov, M. I. Katsnelson, and V. V. Mazurenko, Multiscale structural complexity of natural patterns, *Proc. Natl. Acad. Sci. USA* **117**, 30241 (2020).
- [40] O. M. Sotnikov, I. A. Iakovlev, A. A. Iliasov, M. I. Katsnelson, A. A. Bagrov, and V. V. Mazurenko, Certification of quantum states with hidden structure of their bitstrings, *npj Quantum Inf.* **8**, 41 (2022).
- [41] E. A. Maletskii, I. A. Iakovlev, and V. V. Mazurenko, Quantifying spatiotemporal patterns in classical and quantum systems out of equilibrium, *Phys. Rev. E* **109**, 024105 (2024).
- [42] B. Xiao, J. R. Moreno, M. Fishman, D. Sels, E. Khatami, and R. Scalettar, Extracting off-diagonal order from diagonal basis measurements, *arXiv:2209.10565*.
- [43] R. Blankenbecler, D. J. Scalapino, and R. L. Sugar, Monte Carlo calculations of coupled boson-fermion systems. I, *Phys. Rev. D* **24**, 2278 (1981).
- [44] S. Sorella, S. Baroni, R. Car, and M. Parrinello, A novel technique for the simulation of interacting fermion systems, *Europhys. Lett.* **8**, 663 (1989).
- [45] S. Humeniuk and Y. Wan, Numerically exact mimicking of quantum gas microscopy for interacting lattice fermions, *Phys. Rev. B* **104**, 075155 (2021).
- [46] E. Ibarra-García-Padilla, C. G. Malanche-Flores, and F. J. Poveda-Cuevas, The hobbyhorse of magnetic systems: the Ising model, *Eur. J. Phys.* **37**, 065103 (2016).
- [47] R. T. Scalettar, E. Y. Loh, J. E. Gubernatis, A. Moreo, S. R. White, D. J. Scalapino, R. L. Sugar, and E. Dagotto, Phase diagram of the two-dimensional negative- U Hubbard model, *Phys. Rev. Lett.* **62**, 1407 (1989).
- [48] S. Humeniuk, Generating fermionic pseudo-snapshots, <https://github.com/shumeniuk/fermion-pseudo-snapshots> (2021).
- [49] V. S. Vijayaraghavan, R. G. James, and J. P. Crutchfield, Anatomy of a spin: The information-theoretic structure of classical spin systems, *Entropy* **19**, 214 (2017).
- [50] P. H. Nguyen and M. Boninsegni, Superfluid transition and specific heat of the 2D $x - y$ model: Monte Carlo simulation, *Appl. Sci.* **11**, 4931 (2021).
- [51] Y.-D. Hsieh, Y.-J. Kao, and A. W. Sandvik, Finite-size scaling method for the Berezinskii-Kosterlitz-Thouless transition, *J. Stat. Mech.* (2013) P09001.
- [52] N. Prokof'ev and B. Svistunov, Worm algorithms for classical statistical models, *Phys. Rev. Lett.* **87**, 160601 (2001).
- [53] R. M. Neal, in *Handbook of Markov Chain Monte Carlo*, edited by S. Brooks, A. Gelman, G. Jones, and X.-L. Meng (Chapman and Hall/CRC, New York, 2011), pp. 113–162.
- [54] E. Khatami and M. Rigol, Thermodynamics of strongly interacting fermions in two-dimensional optical lattices, *Phys. Rev. A* **84**, 053611 (2011).

- [55] E. Cocchi, L. A. Miller, J. H. Drewes, C. F. Chan, D. Pertot, F. Brennecke, and M. Köhl, Measuring entropy and short-range correlations in the two-dimensional Hubbard model, *Phys. Rev. X* **7**, 031025 (2017).
- [56] J. Koepsell, D. Bourgund, P. Sompet, S. Hirthe, A. Bohrdt, Y. Wang, F. Grusdt, E. Demler, G. Salomon, C. Gross, and I. Bloch, Microscopic evolution of doped Mott insulators from polaronic metal to Fermi liquid, *Science* **374**, 82 (2021).
- [57] J. Koepsell, S. Hirthe, D. Bourgund, P. Sompet, J. Vijayan, G. Salomon, C. Gross, and I. Bloch, Robust bilayer charge pumping for spin- and density-resolved quantum gas microscopy, *Phys. Rev. Lett.* **125**, 010403 (2020).
- [58] M. Rigol, T. Bryant, and R. R. P. Singh, Numerical linked-cluster approach to quantum lattice models, *Phys. Rev. Lett.* **97**, 187202 (2006).
- [59] B. Tang, E. Khatami, and M. Rigol, A short introduction to numerical linked-cluster expansions, *Comput. Phys. Commun.* **184**, 557 (2013).
- [60] E. Ibarra-García-Padilla, Structural complexity open source code, <https://zenodo.org/records/10268613> (2023).
- [61] P. Corboz, A. M. Läuchli, K. Penc, M. Troyer, and F. Mila, Simultaneous dimerization and SU(4) symmetry breaking of 4-color fermions on the square lattice, *Phys. Rev. Lett.* **107**, 215301 (2011).
- [62] P. Nataf and F. Mila, Exact diagonalization of Heisenberg SU(N) models, *Phys. Rev. Lett.* **113**, 127204 (2014).
- [63] E. Ibarra-García-Padilla, S. Dasgupta, H.-T. Wei, S. Taie, Y. Takahashi, R. T. Scalettar, and K. R. A. Hazzard, Universal thermodynamics of an SU(N) Fermi-Hubbard model, *Phys. Rev. A* **104**, 043316 (2021).
- [64] E. Ibarra-García-Padilla, C. Feng, G. Pasqualetti, S. Fölling, R. T. Scalettar, E. Khatami, and K. R. A. Hazzard, Metal-insulator transition and magnetism of SU(3) fermions in the square lattice, *Phys. Rev. A* **108**, 053312 (2023).
- [65] C. Feng, E. Ibarra-García-Padilla, K. R. A. Hazzard, R. Scalettar, S. Zhang, and E. Vitali, Metal-insulator transition and quantum magnetism in the SU(3) Fermi-Hubbard model, *Phys. Rev. Res.* **5**, 043267 (2023).
- [66] S. Taie, R. Yamazaki, S. Sugawa, and Y. Takahashi, An SU(6) Mott insulator of an atomic Fermi gas realized by large-spin Pomeranchuk cooling, *Nat. Phys.* **8**, 825 (2012).
- [67] C. Hofrichter, L. Riegger, F. Scazza, M. Höfer, D. R. Fernandes, I. Bloch, and S. Fölling, Direct probing of the Mott crossover in the SU(N) Fermi-Hubbard model, *Phys. Rev. X* **6**, 021030 (2016).
- [68] H. Ozawa, S. Taie, Y. Takasu, and Y. Takahashi, Antiferromagnetic spin correlation of SU(N) Fermi gas in an optical superlattice, *Phys. Rev. Lett.* **121**, 225303 (2018).
- [69] S. Taie, E. Ibarra-García-Padilla, N. Nishizawa, Y. Takasu, Y. Kuno, H.-T. Wei, R. T. Scalettar, K. R. A. Hazzard, and Y. Takahashi, Observation of antiferromagnetic correlations in an ultracold SU(N) Hubbard model, *Nat. Phys.* **18**, 1356 (2022).
- [70] D. Tusi, L. Franchi, L. Livi, K. Baumann, D. Benedicto Orenes, L. Del Re, R. Barfknecht, T.-W. Zhou, M. Inguscio, G. Cappellini *et al.*, Flavour-selective localization in interacting lattice fermions, *Nat. Phys.* **18**, 1201 (2022).
- [71] G. Pasqualetti, O. Bettermann, N. Darkwah Oppong, E. Ibarra-García-Padilla, S. Dasgupta, R. T. Scalettar, K. R. A. Hazzard, I. Bloch, and S. Fölling, Equation of state and thermometry of the 2D SU(N) Fermi-Hubbard model, *Phys. Rev. Lett.* **132**, 083401 (2024).
- [72] H. Kim, K. A. Krzyzanowska, K. C. Henderson, C. Ryu, E. Timmermans, and M. Boshier, One second interrogation time in a 200 round-trip waveguide atom interferometer, [arXiv:2201.11888](https://arxiv.org/abs/2201.11888).
- [73] K. A. Krzyzanowska, J. Ferreras, C. Ryu, E. C. Samson, and M. G. Boshier, Matter-wave analog of a fiber-optic gyroscope, *Phys. Rev. A* **108**, 043305 (2023).
- [74] M. Artoni, G. LaRocca, and G. Ferrari, Self-similar scaling in the coherent dynamics of ultracold atoms, *Phys. Rev. A* **80**, 021604(R) (2009).
- [75] G.-B. Jo, J. Guzman, C. K. Thomas, P. Hosur, A. Vishwanath, and D. M. Stamper-Kurn, Ultracold atoms in a tunable optical kagome lattice, *Phys. Rev. Lett.* **108**, 045305 (2012).
- [76] K. Viebahn, M. Sbroscia, E. Carter, J.-C. Yu, and U. Schneider, Matter-wave diffraction from a quasicrystalline optical lattice, *Phys. Rev. Lett.* **122**, 110404 (2019).
- [77] Z. Z. Yan, B. M. Spar, M. L. Prichard, S. Chi, H.-T. Wei, E. Ibarra-García-Padilla, K. R. A. Hazzard, and W. S. Bakr, Two-dimensional programmable tweezer arrays of fermions, *Phys. Rev. Lett.* **129**, 123201 (2022).
- [78] H.-T. Wei, E. Ibarra-García-Padilla, M. L. Wall, and K. R. A. Hazzard, Hubbard parameters for programmable tweezer arrays, *Phys. Rev. A* **109**, 013318 (2024).